

Solid-State Fabrication of Cu₂O/CuO Hydroxide Nanoelectrode Array onto Graphene Paper by Thermal Dewetting for High-Sensitive Detection of Glucose

Antonino Scandurra,* Maria Censabella, Stefano Boscarino, Maria Grazia Grimaldi, Francesco Ruffino,* Guglielmo Guido Condorelli, and Graziella Malandrino

Nanostructures of Cu₂O/CuO hydroxide suitable for the electrochemical determination of glucose are obtained by solid-state dewetting of CuO layers 6, 8, and 31 nm thin deposited by sputtering onto 240 μm-thick graphene paper. Solid-state dewetting in nitrogen produces a partial decomposition of CuO into Cu₂O and Cu. X-ray diffraction patterns reveal the presence of high-index crystallographic facets, which are reactive and useful toward glucose oxidation to gluconolactone. Typically, morphology studied by scanning electron microscopy reveals faceted nanoparticles with an average size below 200 nm. X-ray photoelectron spectroscopy shows that the nanostructure surfaces of Cu₂O and metallic copper exposed to natural ambient are promptly reoxidized and hydroxidized to a mixture of CuO and Cu(OH)₂. Electrochemical characterization in amperometric mode reveals linear response to glucose concentration in the range from 50 to 10 × 10⁻³ M, sensitivity up to 83 μA cm⁻² mM⁻¹, and limit of detection up to 3.6 × 10⁻⁶ M. Good combination of low cost and simplicity of preparation with low limit of detection, high sensitivity, and wide linear range makes the proposed electrodes suitable for a variety of applications ranging from health to food and beverage industries.

1. Introduction

Nanomaterials represent one of the most studied themes of the scientific and technological research of the 21st century. Nanomaterial potentialities have been explored in all the challenging technological fields of the human society.^[1] In fact, nanomaterials having at least one dimension in the nanometer scale present significant unconventional physical and chemical properties with respect to corresponding bulk materials. Nanomaterial properties are of particular interest in the field of electrochemical sensing. In the past years, the use of nanomaterials in combination with electroanalysis techniques has grown considerably.

Several authors reported that some classes of functional nanomaterials exhibit electrocatalyst property or mimic the natural activity of enzymes (enzyme-like activity) and for this reason they are called nanozymes.^[2–5] They possess higher stability and greater availability with respect to natural enzymes.

Nanoscale materials mimicking specific catalytic activity include, but are not limited to, peroxidase,^[6] catalase, glucose oxidase, sulfite oxidase, haloperoxidase, superoxide dismutase (SOD), CO oxidase, laccase, monooxygenase, ferritin ferroxidase,^[7] various hydrolases such as phosphotriesterase phosphatase, carbonic anhydrase, chymotrypsin, as well as endonucleases, DNA-ases, NO synthases, and proteases.^[8–11]


In addition to the mimicking properties of natural enzymes, nanostructures used in combination with electroanalysis techniques show unique advantages over the corresponding large-area electrodes: enhancement of mass transport, catalysis, high effective surface area, and better control of the electrode microenvironment.^[12] Thus, much work has been devoted to their preparation, characterization, and use in the electroanalysis of many electroactive inorganic, organic, and biological species. Important applications based on electroanalysis concern, but are not limited to, the continuous blood glucose monitoring, physiological pH monitoring through sweat, immunosensors assays, heavy metal, and pesticides detection in drinking water. The most used nanomaterials in electroanalysis range roughly from individual carbon-based single- and multiwalled nanotubes

A. Scandurra, M. Censabella, S. Boscarino, M. G. Grimaldi, F. Ruffino
Department of Physics and Astronomy “Ettore Majorana” of University of Catania

via Santa Sofia 64, Catania 95123, Italy
E-mail: ascandurra@unicat.it; francesco.ruffino@ct.infn.it

A. Scandurra, M. Censabella, S. Boscarino, M. G. Grimaldi, F. Ruffino
Institute for Microelectronics and Microsystems of National Research Council of Italy (CNR-IMM)
via Santa Sofia 64, Catania 95123, Italy

G. G. Condorelli, G. Malandrino
Department of Chemical Sciences of University of Catania
Viale Andrea Doria 8, Catania 95123, Italy

 The ORCID identification number(s) for the author(s) of this article can be found under <https://doi.org/10.1002/pssa.202100389>.

© 2021 The Authors. physica status solidi (a) applications and materials science published by Wiley-VCH GmbH. This is an open access article under the terms of the Creative Commons Attribution License, which permits use, distribution and reproduction in any medium, provided the original work is properly cited.

DOI: 10.1002/pssa.202100389

(CNTs), nanoballs, graphene, graphite, or in combination with oxide-hydroxides of elements with partially filled 3 *d* orbital or/and in combination with elements in the state of metals having partially filled 4 *d* and 5 *d* orbitals. Furthermore, applications of various types of elemental and molecular semiconductors are reported.^[13] Nanomaterials can be prepared through a variety of routes that are mainly classified as bottom-up, top-down, physical, biological, and chemical methods.^[13] In the bottom-up process, the manufacturing process involves the building up of the atom or molecular constituents. In contrast, the top-down process involves the atomization of the bulk material through a proper physical or chemical method. The high cost of precious metals used in some electroanalyses can be mitigated by nanoparticle modification of an inexpensive base material.^[14] This approach leads to a larger surface area-to-volume ratio for the precious metal, lowering the final cost of the electrode.^[15] The large effective area of electrode surface is characterized by a large number of active sites, which, in turn, produce an intense electrochemical response and a higher signal-to-noise ratio.^[16] Nonetheless, it should be noted that the voltammetry conducted by the nanoelectrode, where at least one dimension is of the order of nanometers, could imply the change of the diffusive mechanisms of the analyte typically from planar to convergent.^[16] This allows the possibility of exploring electrochemical processes with fast kinetics.^[16]

Nanomaterial synthesis is very dynamic, and the complexity of preparation methods is very large. Some methods commonly used include but are not limited to chemical vapor synthesis, gas condensation, sol-gel technique, mechanical attrition, chemical precipitation, liquid metal ion source, electrodeposition, molecular beam epitaxy, ionized cluster beam, laser beam deposition, electron beam lithography, gas aggregation of monomers, sputtering, chemical precipitation in the presence of capping agents, reaction in microemulsions, and autocombustion.^[17]

Solid-state dewetting of thin films has been proposed for the fabrication of metal nanostructures, with some advantages with respect to other fabrication methods.^[18] Large areas of nanoparticle arrays can be obtained by solid-state dewetting of a film material below the temperature of its melting point.^[19] The solid-state dewetting process depends on several parameters such as material melting point, thermal diffusivity, self-diffusion coefficient, and the initial film thickness. Then, the fabrication of large areas of narrow-spaced nanostructures is very challenging. Often, both the interstitial spacing and the average nanostructure size simultaneously increase as the film thickness increases. Hydrodynamic instability, which occurs when attractive intermolecular forces overcome the stabilizing effect of interfacial tension, produces the dewetting of thin films.^[20] High temperatures amplify the effects of interfacial interactions and metal diffusion, which further complicate dewetting. Moreover, surface processes including chemical interactions and diffusion of metal into the substrate could complicate and influence metal dewetting under conventional long-time annealing. The optimization of the experimental parameters such as film thickness, temperature, and duration of thermal process and substrate is crucial to obtain reproducible dewetting.^[21,22] Laser-assisted dewetting at molten phase has been described in the literature.^[23] The laser-assisted process shows several advantages with respect

to conventional physical and chemical processes, such as green, tunable fabrication in ambient condition and scalability.^[24–27]

In previous papers, we have shown the preparation of electrodes for glucose and fructose determination based on gold nanostructures onto graphene paper (GP).^[28,29] The nanostructures were obtained by two-step fully dry processes consisting of thermal or laser dewetting of thin films of 1.6 and 8 nm of gold deposited by sputtering.^[28,29] The proposed electrodes exhibited competitive analytical performance with the state of the art concerning both enzymatic and nonenzymatic-based electrodes, even at very low metal content up to few percent by atomic surface composition. The proposed processes are characterized by simplicity and low cost, if compared with high throughput.

Copper oxide nanostructures are valid alternatives to gold in glucose sensing. Copper presents three main oxidation states having distinct chemical, electrical, optical properties, and crystalline phases: cupric oxide Cu(II)O with monoclinic crystal structure, cuprous oxide Cu(I)₂O with a cubic crystal structure, and paramelaconite Cu(I)₂Cu(II)₂O₃, a mixture of Cu(II) and Cu(I) coordination, with tetragonal crystal structure.^[30,31] The states of CuO and Cu₂O are the most relevant for chemical sensing both at gaseous phase^[32] and at solution phase by electrochemical methods.^[33] Sun et al. point out the importance of high-index facets in nanostructures of metal oxides, which are characterized by high density of atoms having low coordination.^[34] These nanostructures offer highly active sites for gas sensing and electrochemical applications.^[34] Unfortunately, these facets prepared by conventional wet or biological processes show low stability, even if their preparation is extensively described in the literature.^[35] In previous works, we have emphasized that an approach to enhance the electrocatalytic activity of nanostructures with stable performance is to increase their effective surface area in the form of nanoelectrode array.^[28,29] Then, a further approach to improve the nanostructure electrocatalytic activity consists of the synthesis of them in high-index crystalline or amorphous phases.^[36]

Therefore, the current study aims to shed light on the morphology, surface composition, and crystal structure of CuO_x prepared by the unconventional method consisting of solid-state dewetting of thin films. In detail, we investigated the analytical performance toward glucose electrooxidation of electrodes based on CuO_x nanostructures. The effect of the thickness of the initial CuO layer was investigated. The nanostructures were obtained by thermal dewetting of CuO layer 6, 8, or 31 nm thin, deposited onto GP, and were investigated by Rutherford backscattering spectrometry (RBS), X-ray diffraction (XRD) spectroscopy, scanning electron microscopy (SEM), X-ray photoelectron spectroscopy (XPS), and cyclic voltammetry (CV). The electrocatalytic activities toward glucose oxidation and its amperometric determination in alkali solution for the various thicknesses of CuO are presented and discussed. Our preparation process of CuO_x nanostructure arrays onto GP is based on an easy-to-deploy approach and it is cleanroom friendly and fully dry. The proposed process can be easily integrated at wafer level in the fabrication processes of silicon-based conditioning, amplification, and data logger circuitry. This is of importance for the development of cost-effective and mass-manufacturable compact, user-friendly, and minimally invasive continuous glucose-monitoring devices for mobile and home healthcare.^[37]

2. Results and Discussion

2.1. Morphology Characterization

Morphology and feature size of the CuO_x nanostructured films onto GP were investigated using SEM. **Figure 1a,b** shows the SEM characterization of the CuO_x film 6 nm thick as deposited, obtained at different magnifications. As the CuO_x layer is deposited uniformly, the surface shows typical morphology of the GP alone. Notably, the as-deposited film does not show significant phenomena of aggregation or nucleation characteristic of the early stage of growth of thin metal films.^[28,29]

Morphology of the CuO_x surface dewetted at 500 °C, taken at two different magnifications, is shown in **Figure 1c,d**. The

surface is characterized by high texturing in the presence of dense bright and blunt faceted nanostructures of CuO_x , whose average size is around 200 nm. In addition, we observed thin wires whose chemical nature was no longer investigated. They are likely carbon based rather than CuO_x -based material.

Figure 2a,b shows the morphology of the CuO_x film 8 nm thick as deposited, obtained at different magnifications. Once again, the surface morphology shows typical features of the GP, because the CuO_x layer still exhibits uniform morphology.

Figure 2c,d shows the morphology of CuO_x 8 nm surface dewetted at 500 °C, taken at two different magnifications. Notably, nanowires are not visible, whereas CuO_x nanoparticles exhibit an average size around 200 nm. Moreover, less dense and larger nanoparticles with an average size of 500 nm are observed.

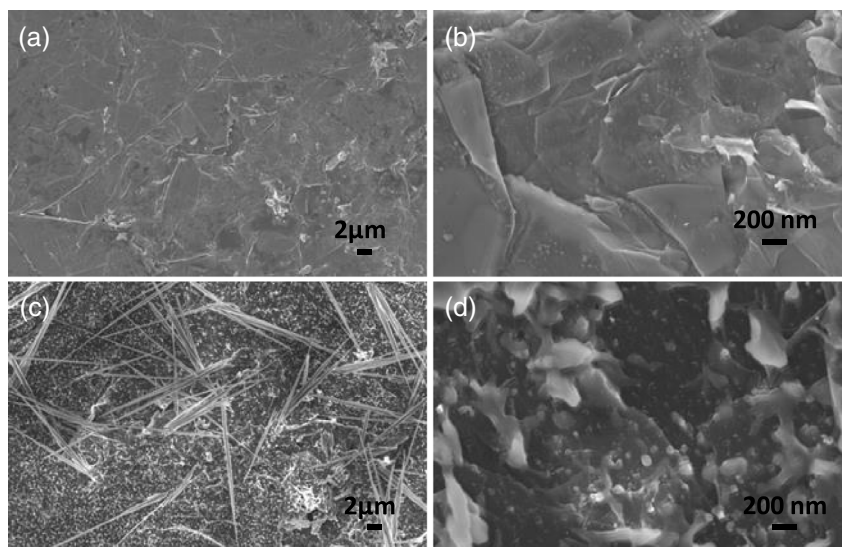


Figure 1. Scanning electron micrographs of CuO 6 nm onto GP: a,b) as deposited and c,d) 500 °C, 1 h, N_2 .

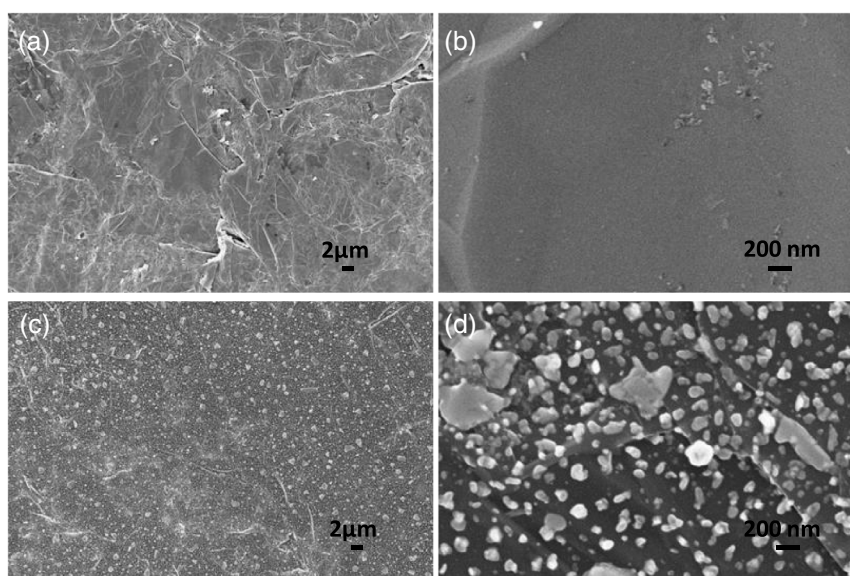


Figure 2. Scanning electron micrographs of CuO 8 nm onto GP: a,b) as deposited and c,d) 500 °C, 1 h, N_2 .

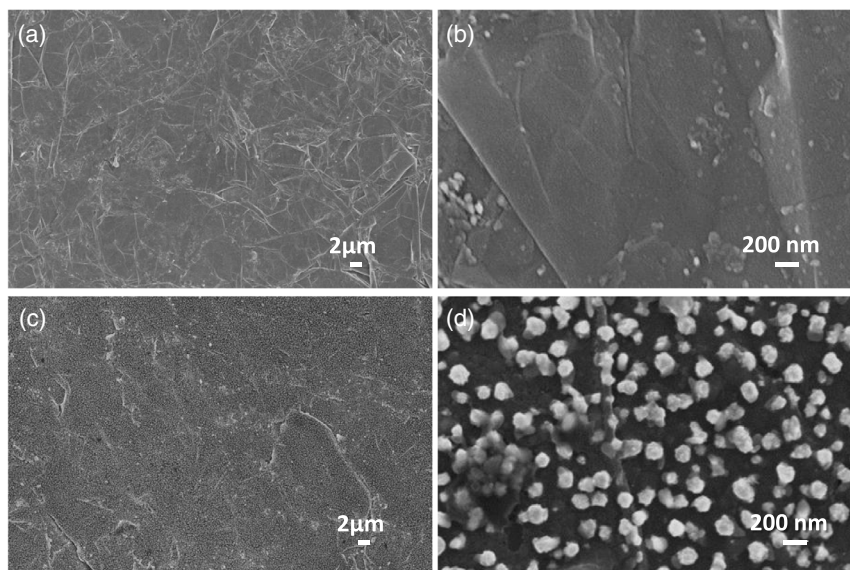


Figure 3. Scanning electron micrographs of CuO 31 nm onto GP: a,b) as deposited and c,d) 500 °C, 1 h, N₂.

Figure 3a,b shows the morphology of the CuO_x film 31 nm as deposited, obtained at different magnifications. The morphology is still uniform and exhibits the typical texturing of the GP.

Nanostructure morphology after dewetting is shown in **Figure 3c,d** at two different magnifications. Dense distribution of nanocrystals, with an average size below 200 nm, is observed. Nanocrystals show typical faceted structures.

2.2. Structural Characterization

Figure 4 shows the RBS spectra of copper observed in CuO_x films at various thicknesses of 6, 8, and 31 nm both in as-deposited state and after thermal dewetting. The spectra of the as-deposited samples show sharp peaks centered at about the channel 605, which in our condition corresponds to He⁺ ions backscattered by copper atoms. The sharpness of the backscattered signal is attributed to the flatness and homogeneity of the films. The spectra were simulated (simulation not shown), assuming a structure of CuO (see later the discussion on XRD characterization) with a density of $4.78 \times 10^{22} \text{ cm}^{-3}$.^[39] The extracted mean values of CuO thicknesses confirmed the nominal values of 6, 8, and 31 nm. In contrast, dewetted samples exhibit significant broadening of the Cu profile, with a tail on the lower side of the channel scale, which is related to the presence of nanocrystals with nonuniform size distribution.

Figure 5 shows the XRD patterns of the 31 nm CuO_x film both in the as-deposited state and after dewetting. The film was deposited both onto silicon single crystals and onto GP. The sample deposited onto silicon single crystals helps in the assignment of the XRD patterns of CuO_x, as there is the interference of the closest peaks of GP at 2θ values of 42.635 and 44.846 that are assigned to the reflection planes 100 and 101 of graphite, respectively.^[40] The as-deposited film onto silicon shows partial overlapped peaks at 2θ values of 35.418 and 35.544, which are assigned to the reflection planes 002 and 11–1, respectively, and at 38.709 assigned to the 111 reflection plane of CuO

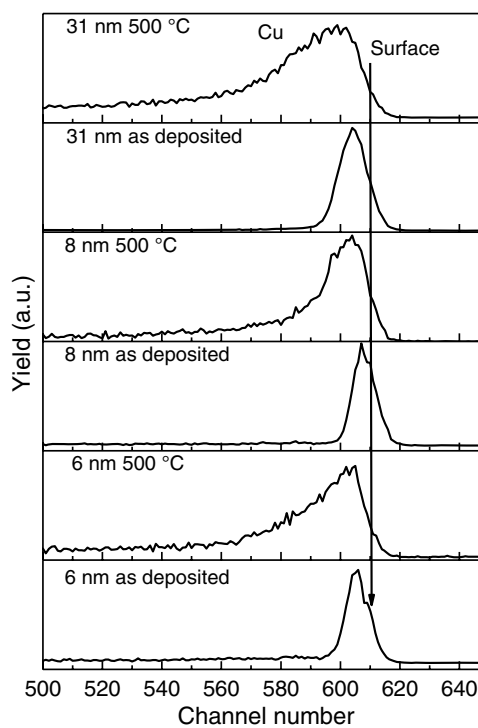


Figure 4. Rutherford backscattering spectra of CuO_x 6, 8, and 31 nm, as deposited and after dewetting at 500 °C, 1 h, N₂.

tenorite.^[41] Dewetted samples show the peaks at 2θ values of 36.419 and 42.298 assigned to the 111 and 200 reflection planes of Cu₂O cuprite, respectively.^[42] Furthermore, a peak at 43.298 assigned to reflection plane 111 of Cu with face-centered cubic crystallinity is observed.^[43] Clearly, the dewetting process produces the partial decomposition of CuO into Cu₂O and Cu, according to Reactions (1) and (2).

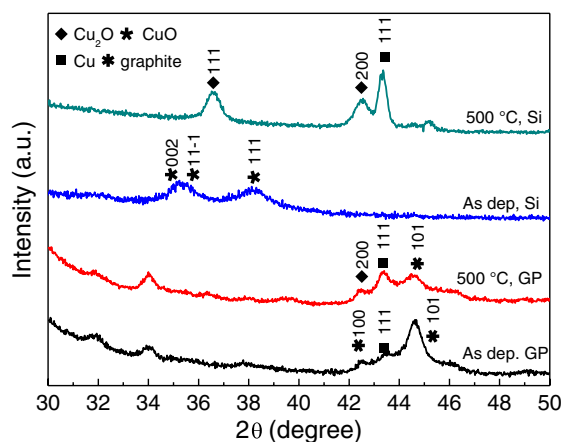


Figure 5. XRD patterns of as-deposited and 500 °C 1 h, N₂-dewetted CuO_x 31 nm onto silicon (Si) and GP, respectively.



At atmospheric oxygen pressure, CuO is a stable phase, but by increasing the temperature (> 1000 °C), Cu₂O phase also becomes stable.^[44] The decomposition process that would not be favorable in atmospheric oxygen pressure at 500 °C takes place during dewetting in nitrogen atmosphere. Reactions (1) and (2) involve the loss of oxygen and the formation of positive vacancies in CuO. Incomplete reconstruction of the CuO crystal at room temperature, in air-exposed samples, leads to the

presence of defect-rich material that is preferable for the electrochemical sensing of glucose. Notably, the film deposited onto GP exhibits less-pronounced peaks with respect to that of single-crystal silicon, as evidenced in the corresponding XRD spectra, which can be explained by the formation of low-crystallinity structures on the former substrate. Moreover, the dewetting process produces nanostructures characterized by surfaces catalytically relevant such as Cu₂O 111 and 200.^[45] Films having thicknesses of 6 and 8 nm did not show significant intensity of the signals attributed to the film structure, maybe because of being too thin or partially amorphous.

2.3. Surface Characterizations

Figure 6a shows comparatively the Cu2p_{3/2} core-level spectra of the pristine (as-deposited) and thermal-dewetted CuO_x films of 6 and 31 nm, respectively. Cu(II) species can be easily distinguished between Cu^o and Cu(I) in XPS by high-intensity shake-up satellite at about 9 eV higher binding energy from the main Cu2p_{1/2} and Cu2p_{3/2} peaks. The broad band of satellite resulting from the shake-up process occurs in the open 3d⁹ shell of Cu(II). The main peaks were deconvoluted by two Gaussian components centered at 933.7–933.8 eV (red line) and 936 eV (green line) of binding energy that are assigned to CuO and Cu(OH)₂ species, respectively.^[46] Notwithstanding XRD revealed the presence of Cu(I) and Cu^o after dewetting of the 31 nm CuO layer, the surface was formed by Cu(II) species and the former species were not detected. As Cu^o and Cu(I) are promptly oxidized to Cu(II), even at room temperature, in air-exposed systems, then, the surface contains mostly the latter species.

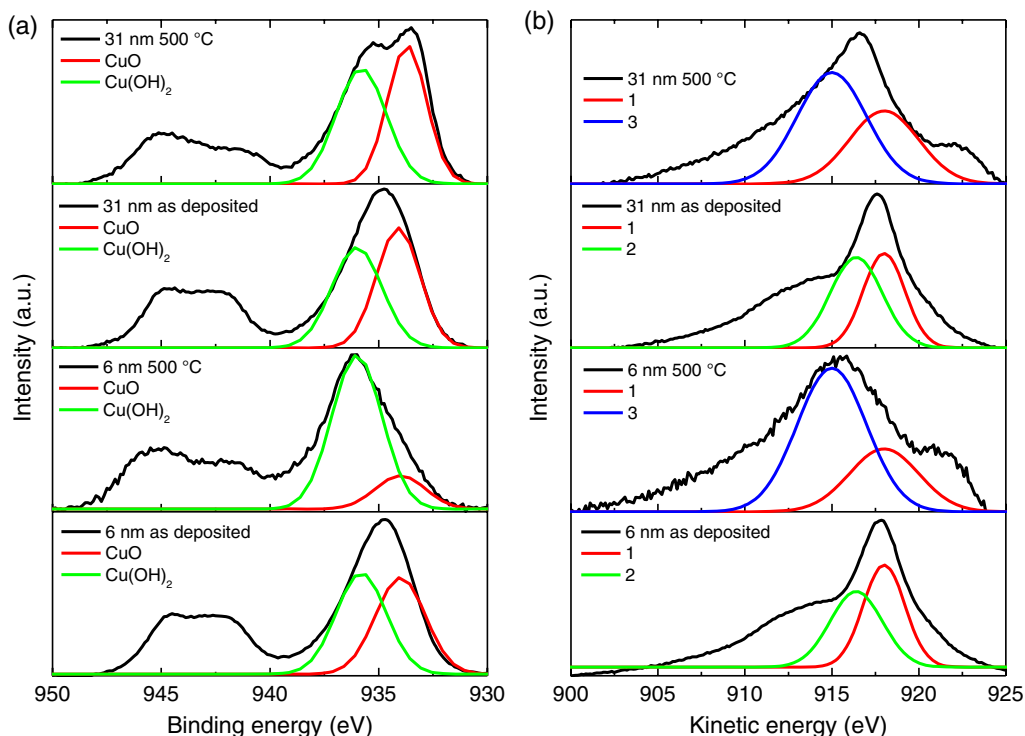


Figure 6. a) Cu2p and b) CuL₃M₄₅M₄₅ spectra of the 6 nm and 31 nm CuO films as deposited and dewetted at 500 °C, 1 h in N₂.

Figure 6b shows the corresponding $\text{CuL}_3\text{M}_{45}\text{M}_{45}$ spectra. Also, the Auger peak is characteristic for Cu(II) and helps further in discrimination among Cu° , Cu(I), and Cu(II) species. The fitting procedure of an Auger peak is not straightforward with respect to photoelectron spectra, being subject to more flexibility, both in the number of used components and in their width. For these reasons several authors leave the Auger peak without deconvolution. Nevertheless, in this work, to help the confirmation of the Cu(II)-based species, we used only two meaningful components. Accordingly, the spectra of Figure 6b were deconvoluted using only two components for each spectrum, centered at 918 eV of kinetic energy, assigned to CuO, and at 916.4 and 915.2 eV of kinetic energy, assigned to two different types of $\text{Cu}(\text{OH})_2$. Notably, $\text{CuL}_3\text{M}_{45}\text{M}_{45}$ peak of $\text{Cu}(\text{OH})_2$ has an intrinsic higher full width at half maximum (FWHM) with respect to that of CuO.^[46] Thus, the spectra of thermal dewetted samples show a more broad Auger peak, reflecting the elevated concentration of hydroxide present in the outermost layers of the surface.

This intrinsic characteristic was taken into account in the FWHM of the Gaussian components. We obtained fittings having an adjusted R^2 ranging from 0.80 to 0.85. The procedure leaves the unfitted portion of the area of the experimental peak, but it can be used because the Auger peak was not used for elemental quantification. **Table 1** shows the corresponding assignments and the $\text{Cu}2p_{3/2}$ - $\text{CuL}_3\text{M}_{45}\text{M}_{45}$ Auger parameter calculated for various samples. According to the nanoscale nature of our CuO_x systems, the values of binding energy and the kinetic energy we found are slightly higher than the literature data based on materials with large-sized structures.^[46] Interface effects in very thin films and nanoscale effects in the nanometer-scale materials can change the expected values of binding energy.^[47,48]

Further information on the surface composition was obtained by analysis of the C1s and O1s core-level spectra shown in **Figure 7a,b**, respectively. The C1s spectrum of the as-deposited CuO sample 6 nm was deconvoluted by three Gaussian components, the first is centered at 284.6 eV of binding energy, and

Table 1. $\text{Cu}2p_{3/2}$ binding energies (eV) and $\text{CuL}_3\text{M}_{45}\text{M}_{45}$ kinetic energies (eV) of CuO and $\text{Cu}(\text{OH})_2$ components. Calculated values of auger parameter ($\text{B.E. Cu}2p_{3/2} + \text{K.E. CuL}_3\text{M}_{45}\text{M}_{45}$) are also reported. The components shown in Figure 6b are indicated by round bracket.

	CuO			Cu(OH) ₂		
	$\text{Cu}2p_{3/2}$ B.E. (eV)	Cu L ₃ M ₄₅ M ₄₅ K.E. (eV)	Auger parameter	$\text{Cu}2p_{3/2}$ BE (eV)	Cu L ₃ M ₄₅ M ₄₅ KE (eV)	Auger parameter
6 nm as deposited	933.8	918 (1)	1851.8	936	916.4 (2)	1852.4
6 nm 500 °C	933.8	918 (1)	1851.8	936	915 (3)	1851
31 nm as deposited	933.8	918 (1)	1851.8	936	916.4 (2)	1852.4
31 nm 500 °C	933.7	918 (1)	1851.7	936	915 (3)	1851

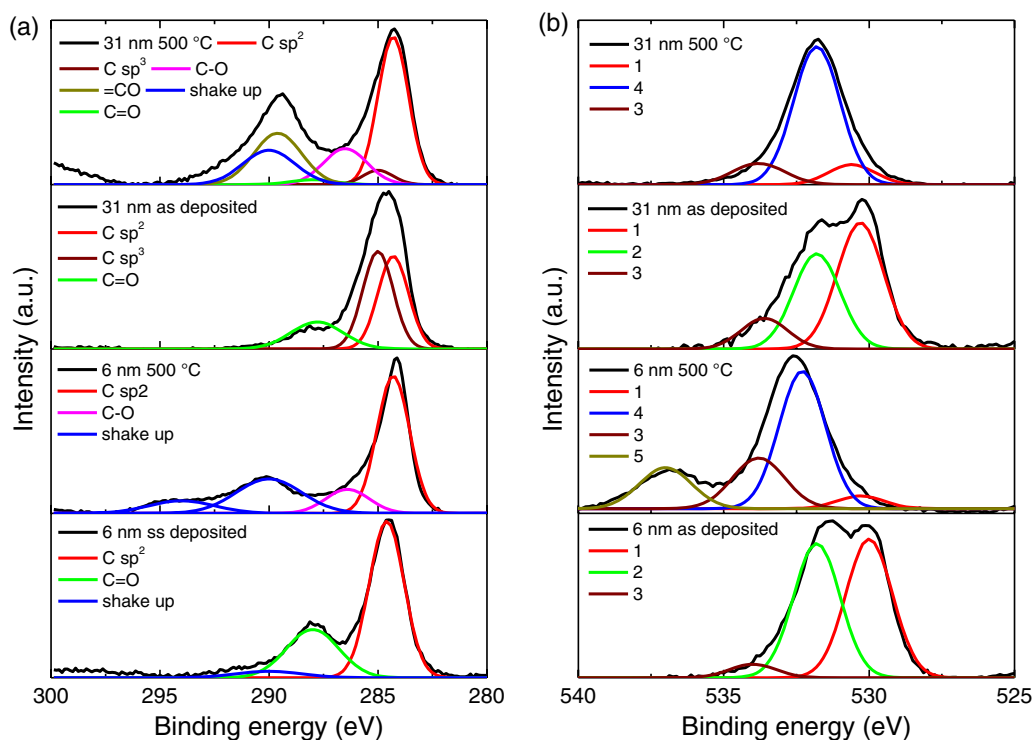


Figure 7. a) C1s and b) O1s X-ray photoelectron spectra of the 6 nm and 31 nm CuO films as deposited and dewetted at 500 °C, 1 h in N_2 .

assigned to sp^2 -hybridized carbon atoms, associated with π -type valence electrons present in the GP. Other two components centered at 288 and 290 eV were assigned to C=O functional group and to the dipole-like $\pi^* \leftarrow \pi$ shake-up transition ($\Delta L = 1$). The spectrum of the sample dewetted shows the components centered at 284.3 and 286.4 eV, assigned to sp^2 -hybridized carbon atoms, and to C–O functional groups derived from oxidation of GP, and 290 and 294 eV, assigned to shake-up satellites, respectively.^[49] The main satellite peaks are found shifted from the core-level peaks at about 5.7 and 9.7 eV, respectively. Remarkable, the former component was found at 4.4 eV in pure highly oriented pyrolytic graphite.^[50] The increase in intensity and the observed shift of the shake-up satellites in the spectra of dewetted samples can be attributed, at least in part, to the interaction of π valence electrons with plasmon excitations in the nanostructure form of CuO/Cu(OH)₂.

The spectrum of 31 nm as-deposited CuO sample shows the components centered at 284.3, 285, and 287.8 eV, assigned to sp^2 -hybridized carbon atoms, adventitious carbon atoms, and to the C=O functional group, respectively. It is worthy of notice in this spectrum that the shake-up satellites were not observed. CuO layer of 31 nm is too thick and prevents the GP substrate from being revealed in XPS. After dewetting, the spectrum shows the component centered at 284.3 (carbon-hybridized sp^2), 285 (adventitious carbon), 286.5 (C–O), 288 (C=O), 289.6 (CuO₂C*=O carbonate), and 290 eV (shake-up), respectively. The shake-up satellites are partially masked by the presence of the component attributed to carbonate.

The spectra of O1s of CuO 6 nm as deposited (Figure 7b) were deconvoluted by Gaussian components centered at 530, 531.8, and 534 eV, assigned to CuO, Cu(OH)₂, and H₂O, respectively. The spectrum of dewetted sample shows the components centered at 530.3, 532.3 eV, assigned to CuO and Cu(OH)₂, and at 533.8 and 537 eV, assigned to H₂O adsorbed onto copper hydroxide and GP, respectively. The spectrum of as-deposited CuO 31 nm shows the components at 530.3, 531.8, and 533.8 eV, assigned once again to CuO, Cu(OH)₂, and H₂O, respectively. The corresponding dewetted sample shows the components at 530.6, 531.8, and 533.8 eV assigned to the previous species.

Table 2 shows the quantitative compositions of such surfaces. The surface copper content in dewetted samples apparently decreases. This finding is related to the minimization of the exposed area of CuO_x nanostructures in dewetted samples, which, in turn, minimizes their interfacial tension and stabilizes them. In addition, the thick layer shows a lower Cu(OH)₂/CuO

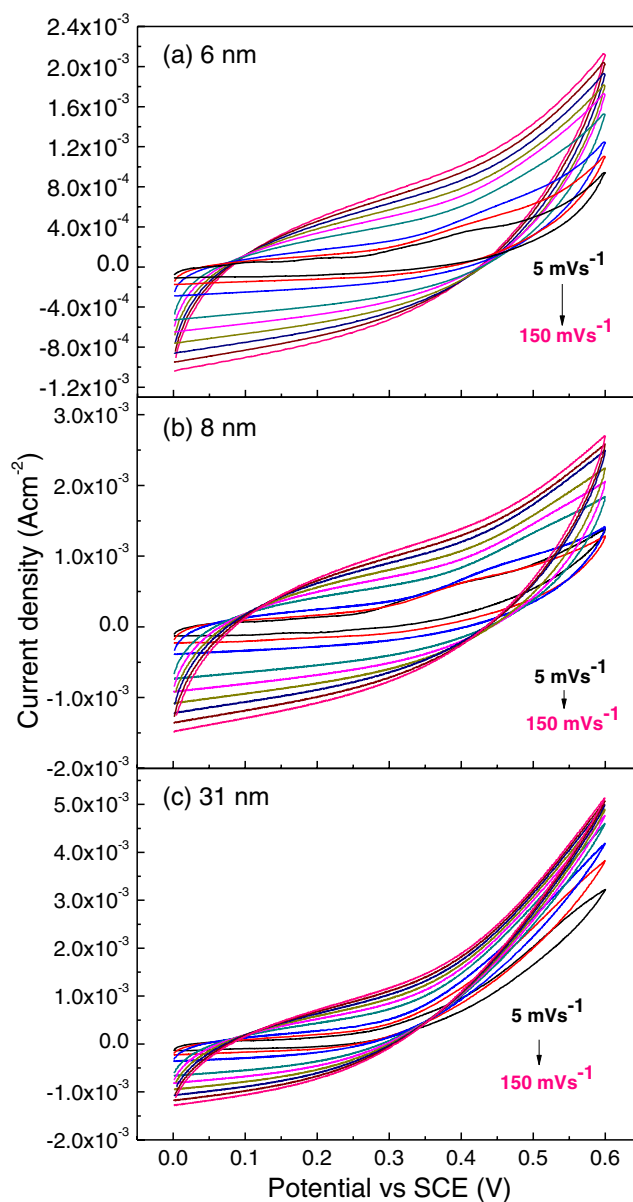


Figure 8. Cyclic voltammograms of glucose 10×10^{-3} M in NaOH 0.1 M at various scan rates obtained by CuO_x 6, 8, and 31 nm thick, respectively.

ratio than the thin layer, where the latter, due the lowest thickness, is easily hydroxidized.

Table 2. Nanostructure elemental compositions by atomic concentration percentage. Corresponding compositions by formula units, derived by the XPS analyses, are also reported.

	Elemental			[Formula units]							
	Cu	O	C	CuO	Cu(OH) ₂	H ₂ O	C sp^2	C sp^3	C–O	C=O	=CO (carbonate)
6 nm as dep	20.7	45.3	34.0	10.1	10.6	2.7	22.7	–	–	11.3	–
6 nm 500 °C	2.8	33.1	64.1	0.5	2.3	14	50.1	–	–	14	–
31 nm as dep	14.8	31.1	54.1	6.9	5.7	3.1	20.3	22.4	–	9.7	–
31 nm 500 °C	6.4	38.8	54.8	3.6	2.9	4.6	27.6	2.6	9.7	1.3	13.8

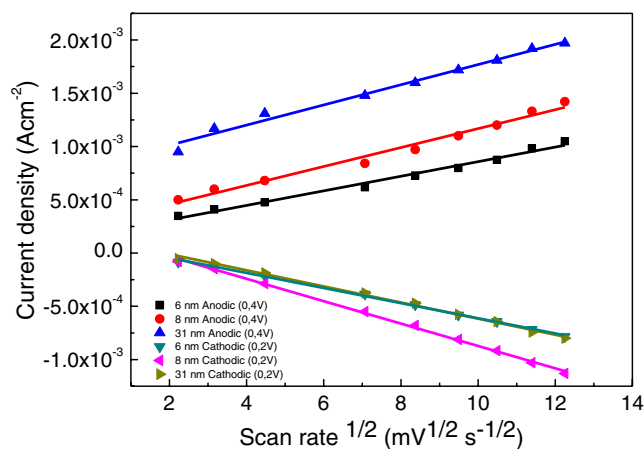


Figure 9. Current density of anodic and cathodic (0.2 V) branches, measured at 0.4 and 0.2 V, respectively, by the voltammograms as a function of square root of scan rate for various thicknesses of initial CuO layer. Condition: glucose 10×10^{-3} M in NaOH 0.1 M.

2.4. Electrochemical Characterization and Glucose Sensing

Electrochemical characterization of electrodes obtained by CuO layers of 6, 8, and 31 nm thin was done by CV in NaOH 0.1 M solution containing 10×10^{-3} M of glucose. **Figure 8a–c** shows such voltammograms in the range of potential from 0 to 0.6 V versus SCE. Current density increases as the scan rate increases from 5 to 150 mV s^{-1} . At a low scan rate, for example, 5 mV s^{-1} , shoulder in the anodic branch is observed at about 0.4 V in all electrodes that is assigned to the process of glucose oxidation to gluconolactone. The observed value is slightly lower than that observed by Sridara and coworkers (at about 0.5 V, corrected for the Ag/AgCl reference) concerning nanocomposite electrode based on carbon nanodots and copper oxide.^[51] The overall shapes of the voltammograms are in good agreement. Notably, our electrodes have a significant current density response, in the range of mA cm^{-2} . Quantitative analyses of the voltammograms furnished further information of the electrode response toward glucose oxidation. In particular, **Figure 9** shows the current density of anodic and cathodic branches, measured at 0.4 and 0.2 V, respectively, by the voltammograms as a function of square root of scan rate. Good linear behavior of the current density versus the square root of the scan rate can be observed, indicating that the oxidation process of glucose by our electrodes is limited by diffusion and it is a surface-confined process. The Equation used for the fitting and the square of the correlation coefficient R^2 are shown in **Table 3**. It is worthy of notice that the anodic current density increases as the initial CuO thickness increases. As the values of the

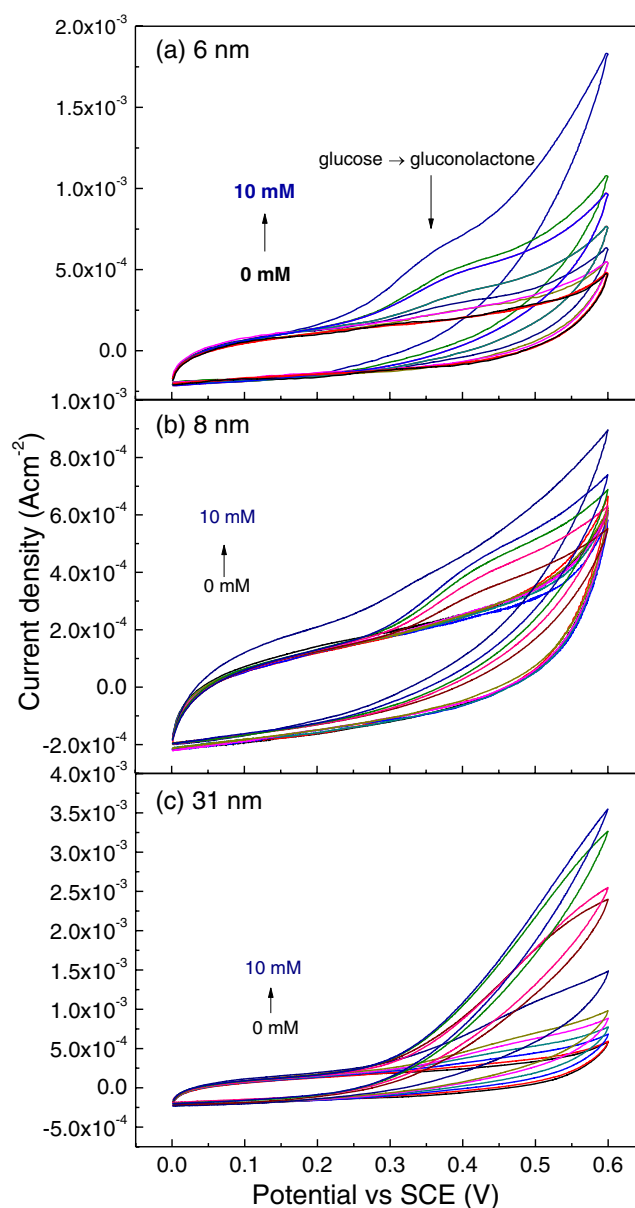


Figure 10. Cyclic voltammograms as a function of glucose concentration obtained by CuO_x 6, 8, and 31 nm thick, respectively. Conditions: scan rate 20 mVs^{-1} ; NaOH 0.1×10^{-3} M.

diffusion and concentration of glucose and temperature present in the Randles Sevcik equation are all the same for the three CuO thicknesses of **Figure 9**, then, the variation of the anodic current is related to the electrode active area, which, in turn, is related to the initial thickness of CuO.

Table 3. Equation and correlation coefficient of current density as a function of square root of scan rate.

CuO _x	Anodic	R^2	Cathodic	R^2
6 nm	$I = 1.7 \times 10^{-4} + 6.9 \times 10^{-5} \nu$	0.9867	$I = 9.8 \times 10^{-5} - 7.1 \times 10^{-4} \nu$	0.9971
8 nm	$I = 2.8 \times 10^{-4} + 8.9 \times 10^{-5} \nu$	0.9810	$I = 1.8 \times 10^{-4} - 10^{-4} \nu$	0.9981
31 nm	$I = 8.2 \times 10^{-4} + 9.9 \times 10^{-5} \nu$	0.9833	$I = 1.4 \times 10^{-4} - 7.6 \times 10^{-4} \nu$	0.9950

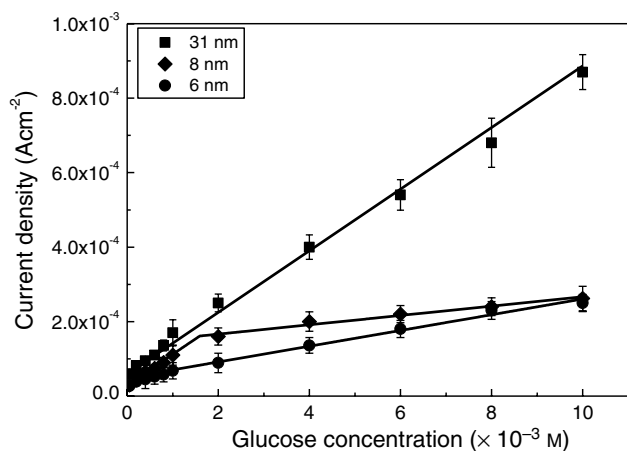


Figure 11. Calibration curves of amperometric detection of glucose by CuO_x 6, 8, and 31 nm-thick electrodes. Conditions: NaOH 0.1 M, potential 0.4 V versus SCE.

Figure 10a–c shows the voltammograms for various glucose concentrations from 0 to 10×10^{-3} M by CuO_x at different thicknesses. The electrodes respond well to the glucose concentration as the anodic current density increases, increasing the glucose concentration.

Notably, the observation of well-defined peaks at 0.4 V, which correspond to glucose oxidation, is limited by depletion of

glucose concentration close to the electrode surface. Glucose depletion at the electrode surface becomes significant as the more efficient convergent diffusion mechanism, rather than planar diffusion, can be hypothesized actively in our nanostructured electrodes. The condition of convergent diffusion is reached when a proper matching of CuO_x nanoparticles' size and their spacings between regions which expose the surface of GP occurs.^[16] The electrocatalytic activity of CuO_x toward glucose oxidation, according to the recent mechanism proposed by Barragan et al.,^[52] is ascribed to the hydroxyl group adsorbed on the positive vacancy of CuO_x that is converted in OH· radicals to positive holes by electrochemical potential, based on the Equation (3).



Then, hydroxyl radicals oxidize glucose molecules to gluconolactone, according to Equation (4). Clearly, the higher the concentration of defects and positive vacancies in CuO_x, as in the high-index crystallographic facets, the higher the efficiency of Reaction (3) and consequently Reaction (4). Calibrations of current density obtained in amperometric mode as a function of glucose concentration are shown in **Figure 11**. The electrodes of CuO_x 6 and 8 nm show linear response from 50×10^{-6} M to 10×10^{-3} M with two sensitivities. The experimental data were fit by piecewise

Table 4. Analytical performances of CuO_x electrodes 6, 8, and 31 nm thin, respectively. for comparison, some recent literature data concerning enzymatic and nonenzymatic sensors based on CuO_x are reported.

Material	Sensitivity ($\mu\text{A cm}^{-2} \text{mm}^{-1}$)	Linear range and fitting equation $J(\text{A cm}^{-2}); c(\times 10^{-3} \text{ M})$	Limit of detection [$\times 10^{-6} \text{ M}$]	Reference
Cu/Cu ₂ O/CSs on GCE	63.8/ 22.6	$0.01\text{--}3.69 \times 10^{-3} \text{ M}$	5	[54]
CuO nanowires on Cu foam	32 330	$0.1 \times 10^{-6} \text{ M}\text{--}0.5 \times 10^{-3} \text{ M}$	0.02	[55]
GO _x /CdS/Gr on GCE	1.76	$2 \text{ mM}\text{--}16 \times 10^{-3} \text{ M}$	700	[56]
CuO _x /GCE	1620	$0\text{--}6 \times 10^{-3} \text{ M}$	49	[57]
PDDA ^{a)} /CuO-C-dots/SPCE	62.3	$0.5\text{--}5 \times 10^{-3} \text{ M}$	200	[51]
CuO _x /Au	3643	$2 \times 10^{-6} \text{ M}\text{--}8.11 \times 10^{-3} \text{ M}$	0.59	[58]
CuO-NPs sphere	–	$5\text{--}600 \times 10^{-6} \text{ M}$	0.59	[59]
CuO _x 6 nm	43	$50 \times 10^{-6} \text{ M}\text{--}1 \times 10^{-3} \text{ M}$ $J = 2.71 \times 10^{-5} + 4.34 \times 10^{-5} c$ $R^2 = 0.9947$	6.9	This work
CuO _x 6 nm	21	$1\text{--}10 \times 10^{-3} \text{ M}$ $= 2.71 \times 10^{-5} + 4.34 \times 10^{-5} c + 2.11 \times 10^{-5} (c - 1)$ $R^2 = 0.9947$	6.9	This work
CuO _x 8 nm	83	$50 \times 10^{-6} \text{ M}\text{--}1.6 \times 10^{-3} \text{ M}$ $J = 2.98 \times 10^{-5} + 8.26 \times 10^{-5} c$ $R^2 = 0.9820$	3.6	This work
CuO _x 8 nm	13	$1.6\text{--}10 \times 10^{-3} \text{ M}$ $J = 2.98 \times 10^{-5} + 8.26 \times 10^{-5} c + 1.25 \times 10^{-5} (c - 1.59)$ $R^2 = 0.9820$	3.6	This work
CuO _x 31 nm	83	$50 \times 10^{-6} \text{ M}\text{--}10 \times 10^{-3} \text{ M}$ $J = 5.91 \times 10^{-5} + 8.28 \times 10^{-5} c$ $R^2 = 0.9932$	3.6	This work

^{a)}CuO: carbon nanodots with poly-(dimethyldiallylammonium chloride).

linear function with two segments whose intersection points are at 1 and 1.6×10^{-3} M of glucose for CuO_x 6 and 8 nm, respectively. In contrast, the electrode of CuO_x 31 nm shows a linear behavior with the same slope (sensitivity) in the entire range from 50×10^{-6} M to 10×10^{-3} M of glucose. In this case, the data were fit by a single linear equation. The fitting parameters, the sensitivity, and the limit of detection of our electrodes are shown in **Table 4**. The limits of detection were calculated based the three times of the current background noise ($3S N^{-1}$) detected in the absence of glucose, divided by sensitivity.^[53] In particular, the limits of detection we obtained are competitive with the literature data and allow glucose determination through saliva or tear. **Table 4** shows some recent literature data concerning both enzymatic and nonenzymatic CuO_x -based glucose sensors. The responses of our electrodes, compared with some recent literature data, combine good sensitivity with a wide linear range and the lowest detection potential (0.4 V). The analytical performances of the proposed electrodes make them suitable for a variety of applications such as health as well as food and beverage industries.

2.5. Interference Study and Electrode Stability

The interference study was done using the thinnest electrode based on CuO 6 nm. Typically, AA and UA are the most common species that interfere in the electrochemical determination of glucose by nonenzymatic-based electrode. In this study, we used AA at the concentrations of 0.25×10^{-3} M and UA at 0.1×10^{-3} M in the determination of 8×10^{-3} M of glucose, in NaOH 0.1 M solution. The concentrations were selected similar to that present in normal human serum. **Table 5** shows the current density variation of glucose determination in the presence of AA and both AA/UA. Negative variations are observed in both cases that can be ascribed to an electrode surface fouling rather than to parasitic electrochemical phenomena.^[60]

Furthermore, the electrode responses were tested up to about 4 months of aging. After a procedure of electrode surface cleaning by three voltammetric cycles in NaOH 0.1 M between 0 and 0.6 V, the electrodes revealed the absence of significant variation in the analytical performances (within 5% of variation of current density at glucose concentration of 8×10^{-3} M).

3. Conclusion

Nanostructures of CuO_x were prepared by thermal dewetting of CuO with various thicknesses. The process of dewetting in nitrogen at 500 °C involves the partial decomposition of CuO into Cu_2O and Cu through the progressive loss of oxygen atoms.

Table 5. Interference study of 0.25×10^{-3} M of AA and 0.1×10^{-3} M of UA in the determination of 8×10^{-3} M of glucose. Condition: CuO_x 6 nm, potential 0.4 V versus SCE.

CuO_x thickness [nm]	Current density (A cm^{-2})	Variation of current density%
GLU	$2.30 \times 10^{-5} \pm 2.6 \times 10^{-6}$	–
GLU + AA	$2.07 \times 10^{-5} \pm 1.6 \times 10^{-6}$	–10
GLU + AA + UA	$1.90 \times 10^{-5} \pm 1 \times 10^{-6}$	–17

Furthermore, air-exposed surfaces of dewetted samples are promptly reoxidized to a mixture of CuO and $\text{Cu}(\text{OH})_2$ at room temperature. As the crystal structure of CuO is not entirely reconstructed, the former processes produce nanometer-scale particles with high-index crystallographic facets and rich positive vacancies. The obtained arrays of nanoparticles are well suited for the electrochemical determination of glucose in alkali media. The proposed fabrication process is very simple, cheap, and green, as the use of numerous reagents required for conventional wet processes are not required. The analytical performances, in particular the sensitivity of the electrodes, are influenced by the initial thickness of CuO explored in the range of 6–31 nm. Obviously, as the initial CuO thickness increases, the concentration of active sites increases, as well as sensitivity. However, even using a CuO layer of 6 nm, the analytical performances are competitive with the existing literature data.

4. Experimental Section

Nanostructure Fabrication and Electrode Preparation: CuO films of different thickness were deposited both onto GP 240 μm thick and onto single crystal Si 100, by sputtering, in Emitech K550X sputter coater. The deposition conditions were 50 mA at ambient temperature, whereas the proper deposition times were selected to obtain nominal thicknesses of CuO of 6, 8, and 31 nm, respectively. The electrodes consisted of a substrate of 1 cm \times 3 cm of GP. Electrodes were fabricated by CuO film deposition onto an area of 1 cm \times 1 cm of the substrate, leaving the remaining portion not covered and used as electrode conductor. The portion of the electrode not covered by CuO and dipped into the analysis solution was isolated by an adhesive tape. Nanostructures of CuO_x were obtained by thermal dewetting in a tubular oven by Carbolite Gero, in N_2 atmosphere, at the condition of 500 °C, 1 h.

Materials: GP 240 μm thick, sodium hydroxide, D-(+)-glucose, uric acid (UA), and ascorbic acid (AA) were purchased from Sigma Aldrich, Milan (Italy). All reagents had an analytical grade and purity of 99.99% or higher and then were used without purifying treatment. Aqueous solutions were made by deionized water treated in a MilliQ system (very low concentration of carbon-based contaminants, $18.2 \text{ M}\Omega \times \text{cm}$). Solutions of glucose at various concentrations were prepared by diluting stock solution of glucose 10×10^{-3} M with NaOH 0.1 M.

Instrumental Characterization: Nanostructure morphology was investigated by SEM. A field-emission Gemini 152 Carl Zeiss Supra 25 instrument was used. Typically, the analyses were conducted by an acceleration voltage of 5 kV and an aperture size of 30 μm , a working distance of 3 mm, and an In-lens detector. 3.5 MV HVEE ((High Voltage Engineering Europa, Netherlands) Singletron accelerator system was used for the RBS measurements. This technique was used to quantify the copper content and characterize the CuO_x nanostructures on the electrodes. The analyses were conducted by 2.0 MeV He^+ beam, at normal incidence, in normal detection modes (165° backscattering angle). RBS spectra were simulated using XRump software,^[38] which furnished the values of CuO_x thickness and amount of copper.

XRD measurements were obtained using a Smartlab Rigaku diffractometer operating in Bragg–Brentano mode. The X-ray source of Cu K α radiation with a rotating anode was operated at 45 kV and 200 mA. Surface chemical composition of nanostructure was studied by XPS. Multitechnique ESCA-Auger PHI 5600 spectrometer was used. The spectra were obtained by Mg K α X-ray source of 1253.6 eV. Typically, the average analyzed area was about 800 μm in diameter. Quantitative compositions of surfaces were obtained by the intensities of the $\text{Cu}2p_{3/2}$, O1s, and C1s peaks, using the corresponding sensitivity factors. Electrochemical measurements were carried out at ambient condition by Versastat 4 Princeton Applied Research potentiostat. Saturated calomel electrode (SCE) and platinum electrode were used

as reference and counter, respectively. Usually, 30 mL of solutions were used for each measurement. The electrocatalytic properties of nanostructures toward glucose determination were studied by CV and current responses in amperometric mode. The measurements were carried out in 0.1 M of NaOH. Before conducting the amperometric response, electrodes were cleaned by three cycles in CV between 0 and 0.6 V in NaOH 0.1 M.

Acknowledgement

This work was supported by the projects “Programma di ricerca di Ateneo UNICT 2020-22 linea 2” and “Sviluppo di tecnologie e sistemi avanzati per la sicurezza dell’auto mediante piattaforme ADAS — ADAS+, cod.ARS01_00459, CUP E66C18000410005.” The authors wish to thank the Bio-nanotech Research and Innovation Tower (BRIT) Laboratory of the University of Catania (grant no. PONa3_00136 financed by the MIUR) for the Smartlab diffractometer facility.

Open Access Funding provided by Università degli Studi di Catania within the CRUI-CARE Agreement.

Conflict of Interest

The authors declare no conflict of interest.

Data Availability Statement

Research data are not shared.

Keywords

copper oxides, dewetting, glucose electrochemical sensing, nanoelectrodes

Received: June 23, 2021

Revised: August 9, 2021

Published online:

- [1] I. Khan, K. Saeed, K. Idrees, *Arabian J. Chem.* **2019**, 12, 908.
- [2] Y. Lin, J. Ren, X. Qu, *Adv. Mater.* **2014**, 26, 4200.
- [3] H. Wei, E. Wang, *Chem. Soc. Rev.*, **2013**, 42, 6060.
- [4] Y. Huang, J. Ren, X. Qu, *Chem. Rev.* **2019**, 119, 4357.
- [5] J. Wu, X. Wang, Q. Wang, Z. Lou, S. Li, Y. Zhu, L. Qin, H. Wei, *Chem. Soc. Rev.*, **2019**, 48, 1004.
- [6] A. Carmona-Ribeiro, T. Prieto, I. L. Nantes, *Front. Mol. Biosci.* **2015**, 2, 50.
- [7] B. Jiang, L. Fang, K. Wu, X. Yan, K. Fan, *Theranostics* **2020**, 10, 687.
- [8] P. Wang, T. Wang, J. Hong, X. Yan, M. Liang, *Front. Bioeng. Biotech.* **2020**, 8, 1.
- [9] M. Liang, X. Yan, *Acc. Chem. Res.* **2019**, 5, 2190.
- [10] D. Jiang, D. Ni, *Chem. Soc. Rev.* **2019**, 48, 3683.
- [11] N. Stasyuk, O. Smutok, O. Demkiv, T. Prokopiv, G. Gayda, M. Nisnevitch, M. Gonchar, *Sensors* **2020**, 20, 4509.
- [12] C. M. Welch, R. G. Compton, *Anal. Bioanal. Chem.* **2006**, 384, 601.
- [13] L. A. Kolahalam, I. V. Kasi Viswanath, B. S. Diwakar, B. Govindh, V. Reddy, Y. L. N. Murthy, *Mat. Today Proc.* **2019**, 18, 2182.
- [14] J. Wang, *Microchim Acta* **2012**, 177, 245.
- [15] D. Martín-Yerga, *Biosensors* **2019**, 9, 47.
- [16] S. J. Hood, D. K. Kampouris, R. O. Kadara, N. Jenkinson, F. Javier del Campo, F. Muñoz, C. E. Banks, *Analyst* **2009**, 134, 2301.
- [17] N. Baig, I. Kammakam, W. Falath, *Mater. Adv.* **2021**, 2, 1821.
- [18] M. Kang, S. Park, K. Jeong, *Sci. Rep.* **2015**, 5, 14790.
- [19] Y. J. Oh, K. H. Jeong, *Adv. Mater.* **2012**, 24, 2234.
- [20] R. Seemann, S. Herminghaus, K. Jacobs, *Phys. Rev. Lett.* **2001**, 86, 5534.
- [21] F. Ruffino, M. G. Grimaldi, *Phys. Status Solidi A* **2015**, 212, 1662.
- [22] F. Ruffino, M. G. Grimaldi, *Appl. Surf. Sci.* **2013**, 270, 697.
- [23] S. Sedaghat, C. Piepenburg, A. Zareei, Z. Qi, S. Peana, H. Wang, R. Rahimi, *ACS Appl. Nano Mater.* **2020**, 3, 5260.
- [24] V. Selvamani, A. Zareei, A. Elkashif, M. Maruthamuthu, S. Chittiboyina, D. Delisi, Z. Li, L. Cai, V. Pol, M. Seleem, R. Rahimi, *Adv. Mat. Interfaces* **2020**, 7, 1901890.
- [25] F. Ruffino, V. Torrisi, R. Grillo, G. Cacciato, M. Zimbone, G. Piccitto, M. G. Grimaldi, *Superlattices and Microst.* **2017**, 103, 28.
- [26] J. Bischof, M. Reinmuth, J. Boneberg, S. Herminghaus, T. Palberg, P. Leiderer, *Proc. SPIE* **1996**, 2777, 119.
- [27] S. Herminghaus, K. Jacobs, K. Mecke, J. Bischof, A. Fery, M. Ibn-Elhaj, S. Schlagowski, *Science* **1998**, 282, 916.
- [28] A. Scandurra, F. Ruffino, S. Sanzaro, M. G. Grimaldi, *Sens. Actuators B Chem.* **2019**, 301, 127113.
- [29] A. Scandurra, F. Ruffino, M. Censabella, A. Terrasi, M. G. Grimaldi, *Nanomaterials* **2019**, 9, 1794.
- [30] A. S. Zoolfakar, R.A. Rani, A.J. Morfa, A.P. O’Mullane, K. Kalantar-Zadeh, *J. Mater. Chem. C* **2014**, 2, 5247.
- [31] B. K. Meyer, A. Polity, D. Reppin, M. Becker, P. Hering, P. J. Klar, T. Sander, C. Reindl, J. Benz, M. Eickhoff, C. Heiliger, M. Heinemann, J. Blasing, A. Krost, S. Shokovets, C. Müller, C. Ronning, *Phys. Status Solidi B* **2012**, 249, 1487.
- [32] S. Steinhauer, *Chemosensors* **2021**, 9, 51.
- [33] Y. Huang, J. Ren, *Chemical Reviews* **2019**, 119, 4357.
- [34] S. Sun, X. Zhang, J. Cui, Q. Yanga, S. Liang, *Nanoscale* **2019**, 11, 15739.
- [35] A. Muthuvel, M. Jothibas, C. Manoharan, *Nanotechnol. Environ. Eng.* **2020**, 5, 14.
- [36] Z. Tian, H. Bai, Y. Li, W. Liu, J. Li, Q. Kong, G. Xi, *ChemistryOpen* **2020**, 9, 80.
- [37] Global Glucose Monitoring System Market Forecast **2019-2028**. Available online: <https://www.inkwoodresearch.com/reports/glucose-monitoring-system-market>, 169, Harrison avenue Boston, MA 02111, (accessed: August 4 2021).
- [38] M. Thompson, Xrump. Available online: www.genplot.com, (accessed: May 2021).
- [39] *Handbook Of Chemistry And Physics* (Ed: D. R. Lide), CRC Press, Boca Raton, FL, USA **2005**.
- [40] J. Howe, C. Rawn, L. Jones, H. Ow, *Powder Diffraction* **2003**, 18, 150.
- [41] J. Langford, D. Louer, *J. Appl. Crystallogr.* **1991**, 24, 149.
- [42] R. Restori, D. Schwarzenbach, *Acta Crystallogr., Sec. B: Structural Science* **1986**, 42, 201.
- [43] H. E. Swanson, E. Tatge, Standard X-ray Diffraction Powder Patterns, Natl. Bur. Stand. (U.S.), Circ. 539, I, 15, (**1953**), <https://nvlpubs.nist.gov>, (accessed: May 2021).
- [44] S. Choudhary, *AIP Advances* **2018**, 8, 055114.
- [45] A. Soon, M. Todorova, B. Delley, C. Stampfl, *Phys. Rev. B* **2007**, 75, 125420.
- [46] M. C. Biesinger, *Surf. Interface Anal.* **2017**, 49, 1325.
- [47] G. Lassaletta, A. Fernández, J. Espinós, A. González-Elipe, *J. Phys. Chem.* **1995**, 99, 1484.
- [48] J. P. Espinós, J. Morales, A. Barranco, A. Caballero, J. Holgado, A. González-Elipe, *J. Phys. Chem. B* **2002**, 106, 6921.
- [49] *Practical Surface Analysis* (Eds: D. Briggs, M.P. Seah) **1**, John Wiley & Sons, Chichester, UK **1990**.
- [50] J. A. Leiro, M. H. Heinonen, T. Laiho, *J. Electron. Spectrosc. Relat. Phenom.*, **2003**, 128, 205.
- [51] T. Sridara, J. Upan, G. Saianand, A. Tuantranont, C. Karuwan, J. Jakmunee, *Sensors* **2020**, 20, 808.

- [52] J. Barragan, S. Kogikoski, E. da Silva, L. Kubota, *Analytical Chemistry* **2018**, *90*, 3357.
- [53] E. Desimoni, B. Brunetti, *Pharm. Anal. Acta.* **2015**, *6*, 355.
- [54] H. Yin, Z. Cui, L. Wang, Q. Nie, *Sens. Actuators B Chem.* **2016**, *222*, 1018.
- [55] X. Liu, W. Yanga, L. Chena, J. Jia, *Electrochim. Acta* **2017**, *235*, 519.
- [56] K. Wang, Q. Liu, Q. Guan, *Biosens. Bioelectron.* **2011**, *26*, 2252.
- [57] C. Li, Y. Su, S. Zhang, X. Lv, H. Xia, Y. Wang, *Biosensors and Bioelectronics* **2010**, *26*, 903.
- [58] M. Guo, P. Wang, C. Zhou, Y. Xia, W. Huang, Z. Li, *Sens. Actuators B Chem.* **2014**, *203*, 388.
- [59] Q. Wu, L. He, Z. Jiang, Y. Li, Z. Cao, C. Huang, Y. Li, *Biosensors and Bioelectronics* **2019**, *145*, 111704.
- [60] D. Branagan, C. B. Breslin, *Sens. Actuators B Chem.* **2019**, *282*, 490.